A 28-GHz Hybrid Beamforming Transmitter With Spatial Notch Steering Enabling Concurrent Dual Data Streams for 5G MIMO Applications

Yaolong Hu, *Graduate Student Member, IEEE*, Xiaohan Zhang, *Graduate Student Member, IEEE*, and Taiyun Chi, *Member, IEEE*

***Abstract*— This article presents a new notch steering scheme for hybrid beamforming transmitters (TXs) aimed at suppressing spatial interference, thereby enhancing the signal-to-interference-plus-noise ratio (SINR) to support spatial multiplexing. Built upon existing phased arrays, this scheme integrates an auxiliary-path vector modulator (VM) into each antenna element, which in turn, forms an interference-canceling beam. By spatially combining the array factors (AFs) of the main beam and the interference-canceling beam, a deep spatial notch is created while ensuring minimal main-beam power degradation. Unlike the conventional zero-forcing method that requires matrix inversion in digital for spatial notch creation, our scheme enables the computation of antenna weights in analog, significantly reducing the computational cost and latency. Leveraging this new notch steering scheme, we develop a 28-GHz four-element fully connected (FC) hybrid beamforming TX array using the GlobalFoundries 45-nm CMOS Silicon-on-Insulator (SOI) process. It is capable of simultaneously transmitting two independent, wideband data streams (DSs) in the same polarization toward two directions. In probing-based measurements, each TX channel delivers 19.7-dBm OP_{1dB}, 20.4-dBm P_{SAT}, and 30.6% peak power-added efficiency (PAE) at 29 GHz, demonstrating state-of-the-art TX linearity and efficiency. In over-the-air (OTA) measurements, the packaged TX array achieves 29.8-dBm $EIRP_{1dB}$ and is able to steer a spatial notch outside the −10-dB beamwidth of the main beam, with a notch depth of >35 dB and a main-beam power degradation of <0.8 dB. Moreover, in spatial multiplexing demonstrations, the TX array is capable of transmitting a 400-MHz 64-quadrature amplitude modulation (QAM) signal to the intended receiver (RX) in the first DS, while suppressing the co-channel continuous-wave or wideband modulated interference created by the second DS with a high SINR.**

***Index Terms*— 5G, CMOS, hybrid beamforming, millimeter wave (mmWave), multiple-input-multiple-output (MIMO), notch steering, phased array, signal-to-interference-plus-noise-ratio (SINR), spatial multiplexing, transmitter (TX).**

Manuscript received 11 November 2023; revised 7 March 2024 and 4 May 2024; accepted 7 May 2024. Date of publication 17 May 2024; date of current version 26 September 2024. This article was approved by Associate Editor Bodhisatwa Sadhu. This work was supported in part by the National Science Foundation under Grant CNS-1956297. *(Corresponding authors: Yaolong Hu; Taiyun Chi.)*

The authors are with the Electrical and Computer Engineering Department, Rice University, Houston, TX 77005 USA (e-mail: yh72@rice.edu; xz82@rice.edu; taiyun.chi@rice.edu).

Color versions of one or more figures in this article are available at https://doi.org/10.1109/JSSC.2024.3399220.

Digital Object Identifier 10.1109/JSSC.2024.3399220

I. Introduction

SPATIAL multiplexing, a technique enabled by antenna arrays, enhances communication throughput by capitalizing on spatial diversity in single-user multiple-input multiple-output (SU-MIMO) [1], [2], [3], or by concurrently transmitting to multiple spatially noncollocated users in multiuser MIMO (MU-MIMO) [4], [5], [6]. When the number of spatial data streams (DSs) is limited (e.g., 2–8), hybrid beamforming, which performs phase shifting at the RF frontend, is a more appealing option than full-digital beamforming. This is because, in a hybrid beamformer, the number of high-speed yet power-hungry data converters is equal to the number of DSs, as opposed to the number of antennas in a digital beamformer.

Two types of hybrid beamforming architectures have been explored: fully connected (FC) hybrid beamforming [7], [8], [9] and partially connected (PC) hybrid beamforming [10], [11]. The FC architecture utilizes all available antennas in the array, thereby preserving the array gain with enhanced energy efficiency compared with the PC architecture. Despite using all antennas, the design complexity of an FC hybrid beamformer remains manageable when handling a limited number of DSs (e.g., ≤8 [12]).

A major challenge of spatial multiplexing is to mitigate spatial interference created by other DSs. One technique to suppress spatial interference and thereby enhance the signal-to-interference-plus-noise ratio (SINR) is notch steering. Several recently reported millimeter wave (mmWave) hybrid beamforming receivers (RXs) have incorporated notch steering. In [11], a four-element RX array is divided into two partially overlapping three-element subarrays to support two concurrent DSs. The notch steering is achieved by adjusting the gain of the variable gain amplifier (VGA) in each channel. In [8], a four-element FC hybrid beamforming RX is reported. The notch steering is accomplished using a minimum mean-square error (MMSE) beam adaptation algorithm, which controls the complex weight of each RF channel. Furthermore, Huang et al. [13], [14] present an eight-element hybrid beamforming RX with a phase-domain feedback mechanism, which autonomously aligns the phase shifters (PSs) toward the incoming signal to achieve either beamforming (if the incoming signal is a desired signal) or notch steering (if the incoming signal is an interference).

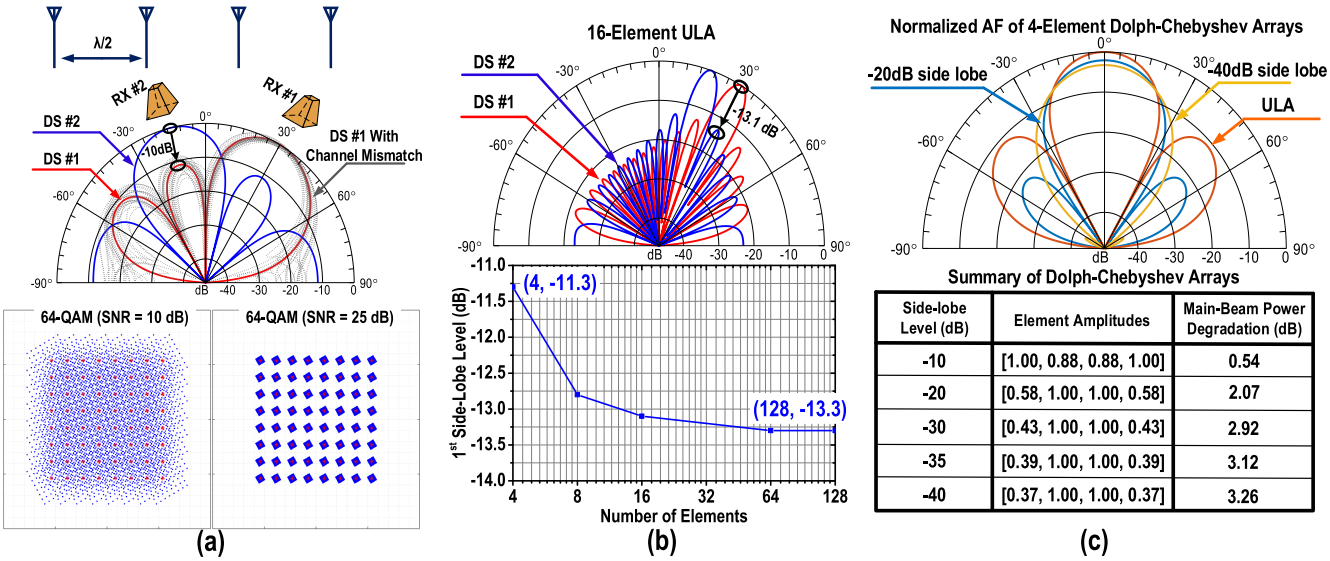

Side-lobe Level (dB)	Element Amplitudes	Main-Beam Power Degradation (dB)
-10	[1.00, 0.88, 0.88, 1.00]	0.54
-20	[0.58, 1.00, 1.00, 0.58]	2.07
-30	[0.43, 1.00, 1.00, 0.43]	2.92
-35	[0.39, 1.00, 1.00, 0.39]	3.12
-40	[0.37, 1.00, 1.00, 0.37]	3.26

Fig. 1. (a) When the sidelobe of DS #1 overlaps with the main lobe of DS #2 for a four-element ULA, the SINR is only ∼10 dB considering channel-to-channel mismatches. Such an SINR is insufficient to demodulate 64-QAM signals. (b) Increasing the number of antennas leads to marginal improvement in sidelobe suppression [15]. (c) Dolph–Cheshev arrays can lower the sidelobe level at the expense of ∼3-dB main-beam power degradation.

In addition to RX-side notch steering, the capability to perform spatial notch steering on the transmitter (TX) side is also crucial. Consider the radiation pattern of a four-element uniform linear array (ULA) in Fig. 1(a), it has a sidelobe level of approximately −10 dB, assuming a ±1-dB amplitude mismatch and a ±10° phase mismatch among the four elements. When the sidelobe of DS #1 overlaps with the main lobe of DS #2, it acts as a strong co-channel interference, limiting the SINR to around 10 dB. Such an SINR is insufficient to demodulate high-order quadrature amplitude modulation (QAM) signals [see Fig. 1(a)]. It is important to note that this sidelobe interference problem cannot be simply solved by increasing the number of antennas. Fig. 1(b) shows that the first sidelobe level improves by only 2 dB, from −11.3 to −13.3 dB, as the number of antennas increases from 4 to 128 [15]. This suggests the necessity of additional techniques for spatial interference suppression.

Dolph–Chebyshev arrays are widely adopted to achieve low sidelobe levels [16]. However, Dolph–Chebyshev arrays require nonuniform element amplitudes. As shown in Fig. 1(c), some elements need to operate in the back-off region, leading to a significant main-beam power degradation. For instance, with a −30-dB sidelobe level, two channels exhibit approximately 60% reduced output amplitude, leading to a close to 3-dB main-beam power degradation.

Various notch steering algorithms have been developed for antenna arrays [17], [18], [19], [20], [21], [22], [23], [24], [25], [26]. Among these, zero-forcing [26] stands out as a prevalent technique in MU-MIMO systems. However, zero-forcing involves matrix multiplication and inversion in the digital domain, resulting in significant power consumption and latency overhead.

To overcome these issues, this article introduces a new notch steering algorithm along with its silicon implementation. This scheme integrates an auxiliary path into each antenna element, which in turn, generates an interference-canceling beam. By spatially combining the array factors (AFs) of the main beam and the interference-canceling beam, a deep spatial notch is created while ensuring minimal main-beam power degradation. Unlike the traditional zero-forcing approach, the proposed algorithm can be efficiently executed in the analog domain within a few clock cycles, thanks to the wide availability of phase-shifting look-up tables in today's phased-array transceivers [27], [28]. In practical implementation, the main and auxiliary paths are realized using two vector modulators (VMs), enabling fine interpolations in the signal I/Q plane. Moreover, the auxiliary-path VM is designed entirely using transistors, ensuring the proposed scheme introduces negligible chip area overhead.

As proof of concept, we implement a 28-GHz four-element TX array using the GlobalFoundries 45-nm CMOS Silicon-on-Insulator (SOI) process [29]. Leveraging the proposed notch steering scheme, the TX array supports two independent DSs with a notch depth of over 35 dB and a main-beam power degradation of less than 0.8 dB in over-the-air (OTA) tests.

The rest of this article is organized as follows. Section II reviews existing notch steering techniques. Section III introduces the proposed notch steering scheme and compares it with existing techniques in terms of main-beam power degradation and practically achievable notch depth. Section IV delves into implementation details of the 28-GHz four-element hybrid beamforming TX. The probing-based and OTA measurement results are presented in Section V. Finally, Section VI concludes this article.

II. Review of Existing Notch Steering Techniques

For an N-element antenna array, up to $N-1$ notches can be introduced by adjusting the complex weight of each element. This can be understood by analyzing the AF of an N-element $\lambda/2$-spaced ULA, given as

$$\mathrm{AF} = \sum_{n=0}^{N-1} e^{jn\Psi} = \sum_{n=0}^{N-1} e^{jn(\pi \sin\theta + \beta)} = \sum_{n=0}^{N-1} z^n \qquad (1)$$

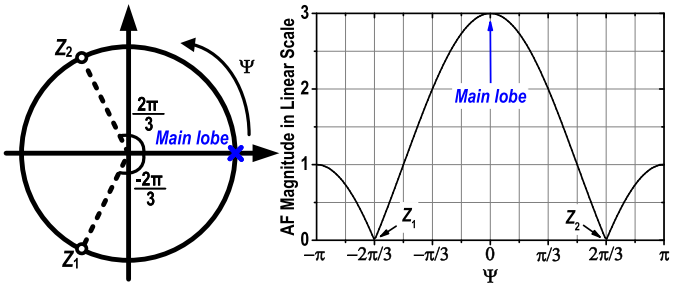

Fig. 2. Three-element ULA has two zeros on the unity circle, corresponding to two spatial notches in its AF.

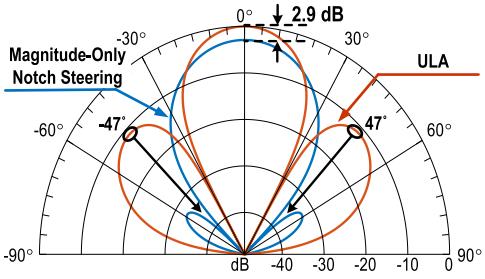

Antenna Element	Magnitude
1st	0.43
2nd	1.0
3rd	1.0
4th	0.43

Fig. 3. Notch steering toward the left sidelobe of a four-element array based on amplitude-only tuning. Note that this method leads to a significant main-beam power degradation of 2.9 dB.

where θ represents the angle of arrival (AoA), β denotes the phase difference between adjacent antennas set by PSs, $\Psi = \pi \sin\theta + \beta$, which is the phase slope of the wavefront, and $z = e^{j\Psi}$. Equation (1) is a polynomial of degree $N-1$ and has $N-1$ zeroes located on the unit circle in the complex plane. These zeroes correspond to spatial notches in the radiation pattern. For instance, as shown in Fig. 2, a three-element ULA has two zeroes on the unit circle (z_1 and z_2), resulting in two notches in the radiation pattern with the main beam pointing to $\Psi = 0°$.

To steer the notches to desired directions, we need to adjust the coefficients of the AF polynomial, as

$$\mathrm{AF} = \sum_{n=0}^{N-1} b_n e^{jn\Psi} = \sum_{n=0}^{N-1} b_n z^n \tag{2}$$

where the coefficients $b_{0,1,2,\ldots,N-1}$ represent the weights assigned to individual antenna elements. Since these weights can be complex values, we can generally divide previously reported notch steering methods into three categories: amplitude-only tuning [17], [18], phase-only tuning [19], [20], [21], and combined amplitude and phase tuning [22], [23], [24], [25], [26]. This section offers an overview of these techniques.

A. Notch Steering Based on Amplitude-Only Tuning

Equation (2) can be reorganized [15], as

$$\mathrm{AF} = \prod_{i=1}^{N-1} (z - z_i) \tag{3}$$

where $z_{1,2,\ldots,N-1}$ represent the zeros of the AF. If only conjugate pair zeros are considered as a solution of (3), then (3) can be further simplified as

$$\mathrm{AF} = \begin{cases} \displaystyle\prod_{i=1}^{(N-1)/2} (z - z_i)\left(z - z_i^*\right), & N \text{ is odd number} \\ \displaystyle (z+1) \prod_{i=1}^{N/2-1} (z - z_i)\left(z - z_i^*\right), & N \text{ is even number.} \end{cases} \tag{4}$$

It is important to note that the conjugate zero pairs in (4) contribute purely real coefficients, as

$$(z - z_i)\left(z - z_i^*\right) = z^2 - 2\cos\Psi_i z + 1. \tag{5}$$

This implies that the coefficients $b_{0,1,2,\ldots,N-1}$ in (2) are all purely real. In essence, notch steering can be achieved by only adjusting the amplitude of each antenna element.

However, amplitude-only notch steering comes at the cost of large main-beam power degradation. This is because some of the channels need to work in the back-off region due to reduced amplitude. For example, in a four-element array, $(b_0, b_1, b_2, b_3) = (1, 1-2\cos\Psi_1, 1-2\cos\Psi_1, 1)$. When steering a notch toward the left sidelobe (i.e., $\theta_1 = -47°$, see Fig. 3), the normalized amplitude becomes (0.43, 1.0, 1.0, 0.43), resulting in a main-beam power degradation of 2.9 dB. It is interesting to note that another notch is simultaneously created at the right sidelobe of $+47°$ due to the conjugate zero pairs.

B. Notch Steering Based on Phase-Only Tuning

It is mathematically complicated to derive a closed-form solution for the phase-only tuning method. Instead, it can be framed as an optimization problem [22], as

$$\begin{cases} min: \displaystyle\sum_{n=0}^{N-1} c_n |b_n e^{j\psi_n} - b_n|^2 & \text{(6a)} \\ \text{s.t: } \mathrm{AF}|_{\theta_0} = \displaystyle\sum_{n=0}^{N-1} b_n e^{j(n\Psi+\psi_n)}|_{\theta_0} = 0 & \text{(6b)} \end{cases}$$

where $b_{0,1,2,\ldots,N-1}$ are predetermined weights assigned to individual antennas in the absence of notch steering, θ_0 represents the desired notch direction, and $\psi_{0,1,2,\ldots,N-1}$ represent the phase tuning applied to the antennas. Equation (6b) ensures the AF forms a notch in the desired direction, while (6a) guarantees minimal deviation from the original antenna weight. Coefficients c_n are introduced to allow flexibility to this optimization problem.

Overall, (6) outlines a nonlinear optimization problem. For scenarios where the phase tuning ψ_n is small, the equation can be linearized, and an analytical solution to this linear approximation is detailed in [20]. If we apply this technique to steer a notch toward the left sidelobe of a four-element array, the sidelobe indeed gets attenuated, with a main-beam power degradation of 0.7 dB [see Fig. 4(a)]. However, the achieved notch direction shifts from the desired $-47°$ to $-50.5°$ due to the linear approximation. Kajenski [21] introduces another method based on semidefinite program to approach (6) without the need for linear approximation. As a result, the notch can be precisely placed in the desired direction [see Fig. 4(b)].

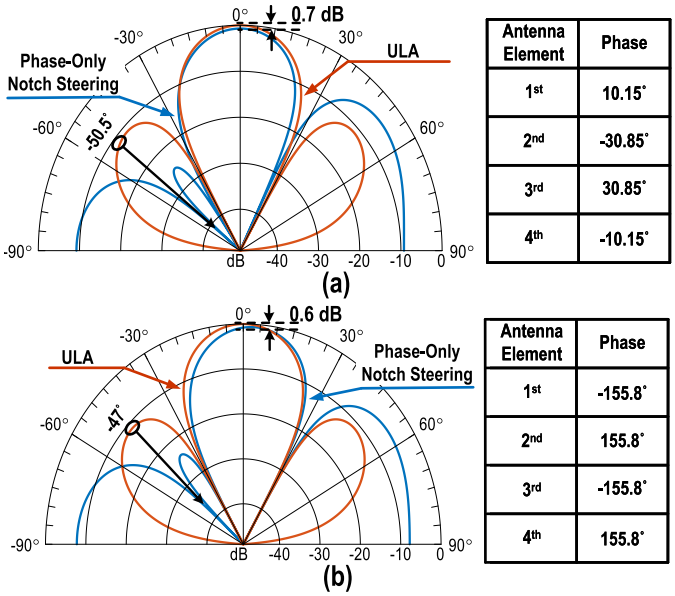

Antenna Element	Phase
1st	10.15°
2nd	-30.85°
3rd	30.85°
4th	-10.15°

Antenna Element	Phase
1st	-155.8°
2nd	155.8°
3rd	-155.8°
4th	155.8°

Fig. 4. Notch steering toward the left sidelobe of a four-element array based on phase-only tuning, using (a) linear approximation method [20] and (b) semidefinite program method [21]. Note that both methods lead to a significantly stronger sidelobe on the right.

However, it is worth noting that both methods lead to a significantly stronger sidelobe on the right, with a sidelobe level of −5.1 and −5.2 dB, respectively.

C. Notch Steering Based on Combined Amplitude and Phase Tuning

Employing both amplitude and phase tuning brings more degrees of freedom for notch steering. There exist several methods for determining the desired amplitude and phase for each antenna element [23], [24], [25]. One notable method is zero-forcing [26].

In zero-forcing, the complex weight $\boldsymbol{W}$ is derived as the pseudoinverse of the channel matrix $\boldsymbol{H}$, as

$$\boldsymbol{W} = (\boldsymbol{H}^{\boldsymbol{H}}\boldsymbol{H})^{-1}\boldsymbol{H}^{\boldsymbol{H}}. \tag{7}$$

Here, $(\cdot)^{\boldsymbol{H}}$ denotes the Hermitian transpose, and $\boldsymbol{H} = [\boldsymbol{h_1}, \boldsymbol{h_2}, \ldots, \boldsymbol{h_k}]$ represents the $N \times K$ channel matrix for K users. For a line-of-sight (LOS) channel, $\boldsymbol{h_k} = [1, e^{j\beta_k}, \ldots, e^{(N-1)j\beta_k}]^T \in \mathbb{C}^{N\times 1}$, which is the same as the classic beam steering vector of a ULA.

It is important to recognize that zero-forcing involves matrix multiplication and inversion. Although the complex weight $\boldsymbol{W}$ can be realized at the transceiver frontend using VGA and PS, the computation of $\boldsymbol{W}$ can only be performed in the digital backend. This digital computation can incur high power consumption and latency.

Two notch steering examples using the zero-forcing method for a four-element array and a 16-element array are shown in Fig. 5(a) and (b), respectively. When the notch is created in the first sidelobe direction, the resulting main-beam power degradation is 1.73 dB for the four-element array [see Fig. 5(a) and (c)]. This power degradation plateaus at ∼2.0 dB as the array size increases up to 128 elements, which is due to the sidelobe level becoming saturated at ∼−13.3 dB

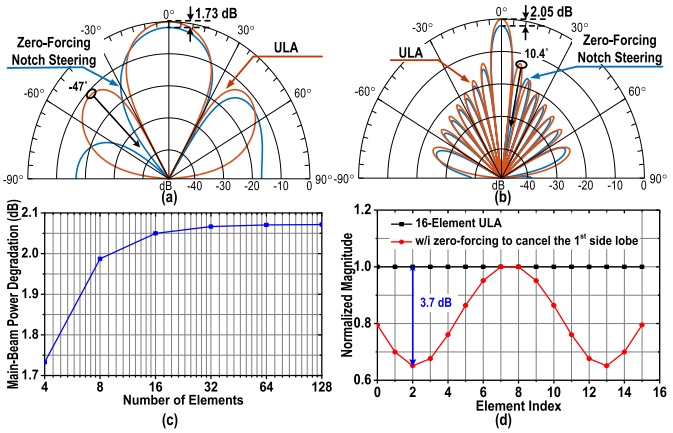

Fig. 5. Using zero-forcing to cancel the first sidelobe of (a) four-element array and (b) 16-element array. (c) Main-beam power degradation versus the number of antenna elements. (d) Normalized amplitudes of the 16-element array after applying zero-forcing.

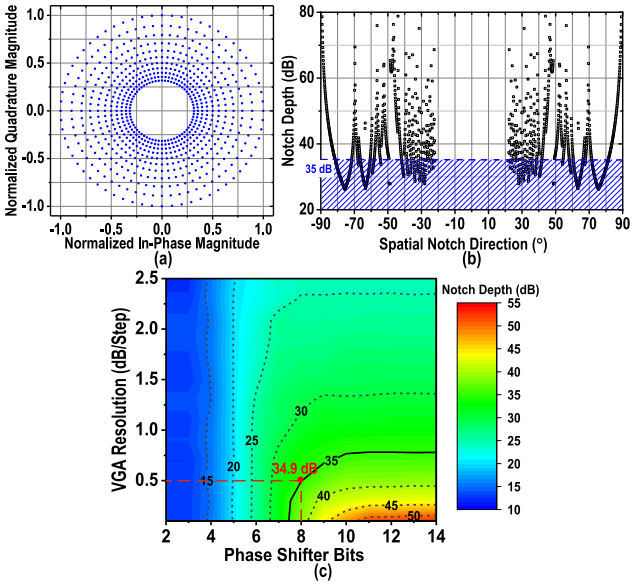

Fig. 6. (a) All selectable complex weights using an ideal 6-bit PS paired with a VGA with a 10-dB tuning range and a 1-dB/step amplitude resolution. (b) Achieved notch depth versus notch direction (outside the −10-dB beamwidth) for a four-element array using zero-forcing. (c) Notch depths under different VGA and PS resolutions using zero-forcing.

with increased element count [see Fig. 1(c)]. Fig. 5(d) plots the normalized amplitudes for the 16-element array after applying the zero-forcing. The minimum element amplitude is ∼0.65× (equivalent to −3.7 dB).

D. Notch Steering Performance Evaluation Using Digitally Controlled VGA and PS With Finite Resolution

In mmWave arrays, amplitude scaling and phase shifting for each antenna element are typically achieved using digitally controlled VGA and PS, respectively. This section investigates the impact of finite tuning range and resolution of the VGA and PS on the achievable notch depth. Since combined amplitude and phase tuning usually outperforms amplitude-only or phase-only tuning, zero-forcing is used here as a demonstration vehicle.

Fig. 6(a) illustrates all selectable complex weights in the I/Q plane, assuming a 6-bit PS (which provides a phase tuning

resolution of 5.625°) paired with a VGA with a 10-dB tuning range and a 1-dB/step amplitude resolution. These are all reasonable assumptions based on recently published mmWave beamformers at 28 GHz [30], [31], [32], [33], [34]. With these parameters, Fig. 6(b) plots the achieved notch depth versus the notch direction for a four-element array using zero-forcing. Here, we assume the main beam is pointed toward 0° and the notch is steered outside the −10-dB beamwidth (−22° to 22° for a four-element array). Due to limited resolutions of the PS and VGA, the worst-case notch depth is only 26.1 dB [see Fig. 6(b)], which barely meets the required SINR for demodulating 64-QAM signals. Furthermore, when steering the notch from ±22° to ±90°, 36.3% of the angular region suffers from notch depths less than 35 dB.

The achievable notch depth can be increased by improving the resolutions of the VGA and PS, as demonstrated in Fig. 6(c). In Fig. 6(c), we also highlight the required VGA and PS resolutions in order to achieve 35-dB notch depth. Setting the VGA resolution to 0.5 dB/step necessitates an 8-bit PS, corresponding to 1.4° phase tuning resolution. Such a high-resolution requirement is clearly nontrivial for practical implementations at mmWave.

III. Proposed Notch Steering Scheme Using a Set of Auxiliary-Path Vector Modulators

A. Adding an Auxiliary Path for Notch Steering

To enable notch steering weight computation in analog, while achieving a large notch depth without the need for high-resolution PS, we propose a new notch steering scheme by introducing an auxiliary path to each antenna element, as shown in Fig. 7(a). Here, the main beam is directed toward the desired direction using the main-path PSs, similar to a conventional phased array. On top of that, an auxiliary path is used to generate a second beam, namely the interference-canceling beam. This interference-canceling beam has the same amplitude but a 180° phase shift compared to the main beam in the notch direction. By spatially combining the AFs of the main beam with the interference-canceling beam in the far-field, a spatial notch can then be generated [29].

For an N-element linear array, the overall AF of the spatially combined main beam and interference-canceling beam can be derived as

$$\begin{aligned}\mathrm{AF_{tot}} &= \sum_{n=0}^{N-1} e^{jn\Psi} + \xi \sum_{n=0}^{N-1} e^{jn\Phi} \\ &= \sum_{n=0}^{N-1} e^{jn(\pi \sin\theta+\beta)} + \xi \sum_{n=0}^{N-1} e^{jn(\pi \sin\theta+\alpha)} \end{aligned} \tag{8}$$

where ξ and α represent the amplitude scaling factor and phase gradient of the auxiliary path, respectively.

If the desired notch direction is denoted as θ_0, (8) should be equal to zero at θ_0. Consequently, the required scaling factor ξ can be found as

$$\begin{aligned}&\mathrm{AF_{tot}\ at\ } \theta_0 = 0 \\ &\Rightarrow \xi = -e^{j\frac{N-1}{2}(\beta-\alpha)} \times \frac{\mathrm{sinc}\left[N\frac{\beta-\alpha}{2\pi}\right]}{\mathrm{sinc}\left[\frac{\beta-\alpha}{2\pi}\right]}. \end{aligned} \tag{9}$$

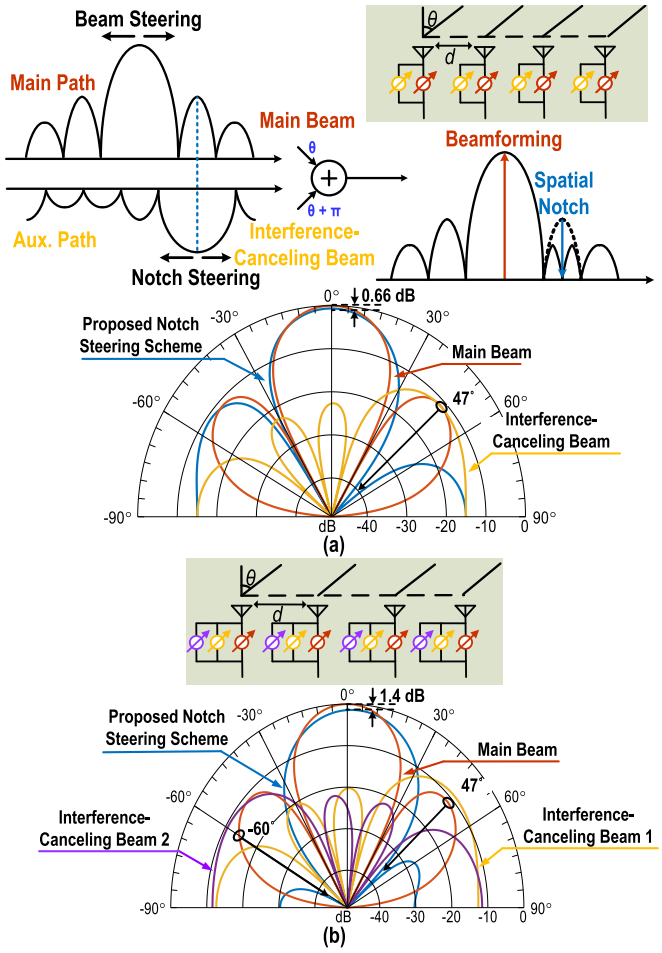

Fig. 7. Proposed notch steering scheme to realize (a) notch in the right sidelobe direction (47°) and (b) two notches in two different directions (47° and −60°).

Upon substituting ξ from (9) into (8), the resulting overall AF in the main-beam direction (θ_m) is given as

$$\mathrm{AF_{tot}\ at\ } \theta_m = N\left[1 - \left(\frac{\mathrm{sinc}\left[\frac{N(\beta-\alpha)}{2\pi}\right]}{\mathrm{sinc}\left[\frac{\beta-\alpha}{2\pi}\right]}\right)^2\right]. \tag{10}$$

To steer the notch outside the −10-dB beamwidth, the maximum scaling factor ($\xi_{\max}$) is calculated to be 0.32. In our prototype implementation (see details in Section IV), ξ is designed to be 0.4 to leave some margin.

Other than notch steering, this scheme may also find applications in dual-polarization arrays [35], [36], [37] to enhance the cross-polarization level.

B. Scalability and Main-Beam Power Degradation

Additional auxiliary paths can be added if more spatial notches are needed. As shown in Fig. 7(b), two notches toward different directions can be synthesized using two auxiliary paths. To facilitate the integration of auxiliary paths, their implementation has to be compact. To achieve this, we come up with a scheme that allows the auxiliary path to be designed only using transistors without passive elements. The design details are presented in Section IV-A.

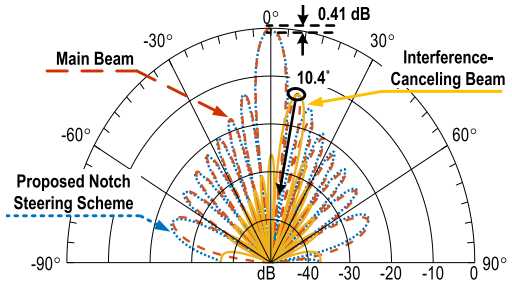

Fig. 8. Demonstration of the proposed scheme to steer a notch toward the first sidelobe direction of a 16-element array.

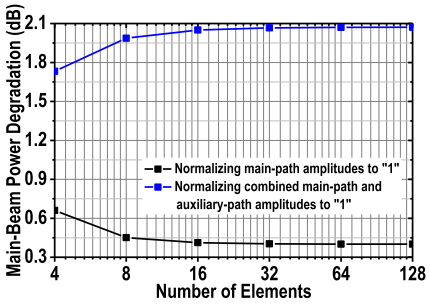

Fig. 9. Main-beam power degradation of the proposed notch steering scheme versus the number of antenna elements.

The proposed notch steering scheme also remains effective when scaling up the number of antennas. Fig. 8 shows the AF of a 16-element array when a notch is steered toward the first sidelobe. A deep spatial notch is created with a main-beam power degradation of only 0.41 dB.

In terms of main-beam power degradation, the largest degradation happens when the notch is steered toward the first sidelobe [see Fig. 7(a)]. In this scenario, the main beam is aligned with the sidelobe of the interference-canceling beam, which is at least 20 dB lower than the main beam, leading to negligible power degradation. Mathematically, the direction of the first sidelobe (θ_{SL1}) can be approximated as

$$\theta_{\mathrm{SL1}} \approx \sin^{-1}\left(\frac{3}{N} - \frac{\beta}{\pi}\right) \tag{11}$$

resulting in a maximum main-beam AF degradation of

$$\frac{\mathrm{AF_{tot}\ at\ }\theta_m}{N}\Big|_{\mathrm{AF_{tot}\ at\ }\theta_{\mathrm{SL1}}=0} \approx 1 - \left[\frac{\mathrm{sinc}\left(\frac{3}{2}\right)}{\mathrm{sinc}\left(\frac{3}{2N}\right)}\right]^2. \tag{12}$$

For a four-element array, this degradation is only 0.65 dB. This 0.65-dB loss assumes the main-path amplitudes are normalized to "1." However, adding the auxiliary path may alter the maximum amplitude per element. To account for this, Fig. 9 plots the maximum main-beam power degradation under two scenarios: when the main-path amplitudes are normalized to "1," and when the combined main-path and auxiliary-path amplitudes are normalized to "1." In the latter scenario, our scheme achieves 1.73-dB main-beam power degradation, which is equivalent to that of the zero-forcing scheme.

C. Comparison With Zero-Forcing

In this section, we present a comparison between the proposed notch steering scheme and the conventional zero-forcing method. We consider a four-element linear array, with its main beam pointed toward 0° and a notch steered outside the −10-dB beamwidth.

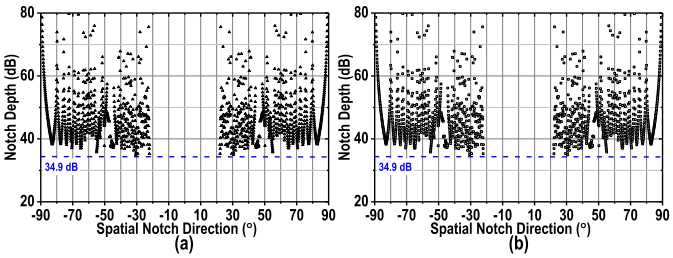

Fig. 10. Achievable notch depth versus notch direction for a four-element array using (a) zero-forcing scheme and (b) our proposed scheme. Both schemes use an identical setup of an 8-bit PS and a VGA with an amplitude resolution of 0.5 dB/step.

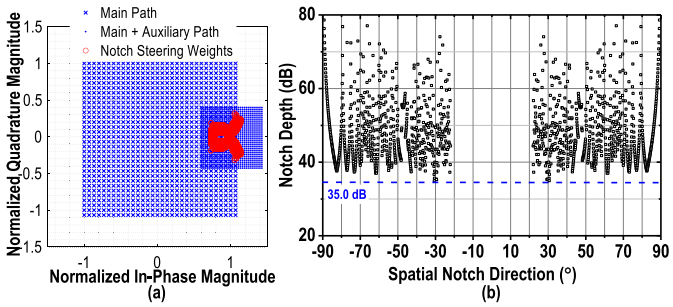

Fig. 11. (a) Complex weights of the main-path and the auxiliary-path VMs, where the auxiliary-path weights are overlaid onto (1, 0), which is the desired main-path weight for steering the main beam to 0°. (b) Achieved notch depth for a four-element array using the complex weights highlighted in (a).

From Figs. 6(c) and 10(a), it can be seen that with a 0.5-dB/step amplitude resolution and an 8-bit PS, the zero-forcing scheme achieves a worst-case notch depth of 34.9 dB. If we combine the main-path weight and auxiliary-path weight as a single complex weight using (8), our scheme achieves an equivalent notch depth under the same VGA and PS resolutions [see Fig. 10(b)]. This result demonstrates the effectiveness of our algorithm assuming the same VGA and PS implementation as zero-forcing.

However, it is important to recognize that the zero-forcing algorithm requires matrix multiplication and inversion in the digital domain to determine the antenna weight, introducing large power consumption and latency. In contrast, for the proposed approach, the weights of the main and auxiliary paths (i.e., their respective phase shifts) can be computed separately using (8), and this computation can be efficiently realized on-chip [28] by leveraging phase-shifting look-up tables that are commonly available in today's phased-array frontends. Consequently, the overall computational cost and latency of our proposed scheme are significantly lower.

D. Implementing Main and Auxiliary Paths Using Vector Modulators

As mentioned in Section III-C, to realize a 35-dB notch depth using the conventional setup requires an 8-bit PS (equivalent to a phase tuning resolution of 1.4°), posing a significant design challenge. Therefore, we propose to realize

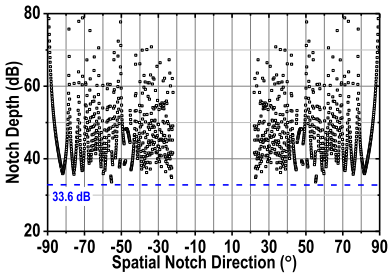

Fig. 12. Notch depth achieved using a 6-bit VM without the auxiliary path. The worst-case notch depth is 1.4 dB lower than that achieved when an auxiliary path is introduced.

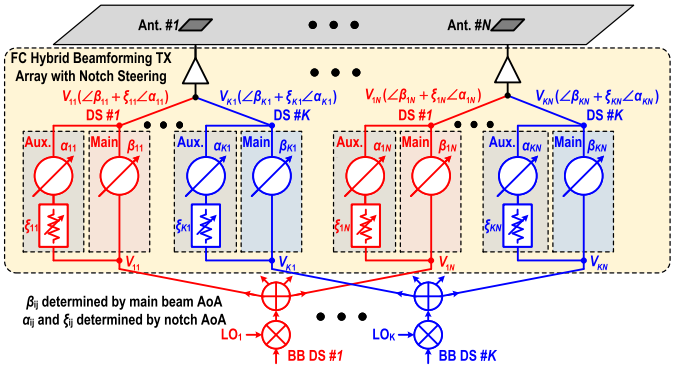

Fig. 13. TX architecture with the proposed notch steering scheme.

the main-path and auxiliary-path complex weights using two VMs. To illustrate this, we overlay the complex weights of the auxiliary-path VM onto those of the main-path VM, as shown in Fig. 11(a), assuming a 5-bit resolution for each VM. In this plot, we scale the maximum main-path weight to "1" and highlight all possible weights for steering a notch outside the −10-dB beamwidth. It can be seen that implementing the auxiliary path using a VM enables finer interpolations in the I/Q plane, thereby effectively reducing the quantization error. Using this setup, we achieve a notch depth of >35 dB, as shown in Fig. 11(b).

Moreover, it is important to note that introducing an auxiliary-path VM is more effective than simply increasing the bit resolution of the main-path VM. As shown in Fig. 12, employing a 6-bit VM without the auxiliary path results in a smaller achievable notch depth of only 33.6 dB. To realize the desired 35-dB notch depth, we need to increase the VM's effective number of bits (ENOB) to 7 bits or more, which is challenging to implement in practice.

IV. Implementation Details of the 28-GHz Hybrid Beamforming TX Prototype

To demonstrate the proposed notch steering scheme, we implement a 28-GHz hybrid beamforming TX array [29]. The TX architecture is shown in Fig. 13. It is designed to support K independent DSs, with each DS routed to all N antennas in an FC fashion. In our proof-of-concept demonstration, $K = 2$ and $N = 4$. V_{ij} denotes the RF input signal for the DS #i at the jth channel. Within the jth RF channel, the main-path VM realize the desired beamforming, while the auxiliary-path VM achieve the notch steering. Their combined

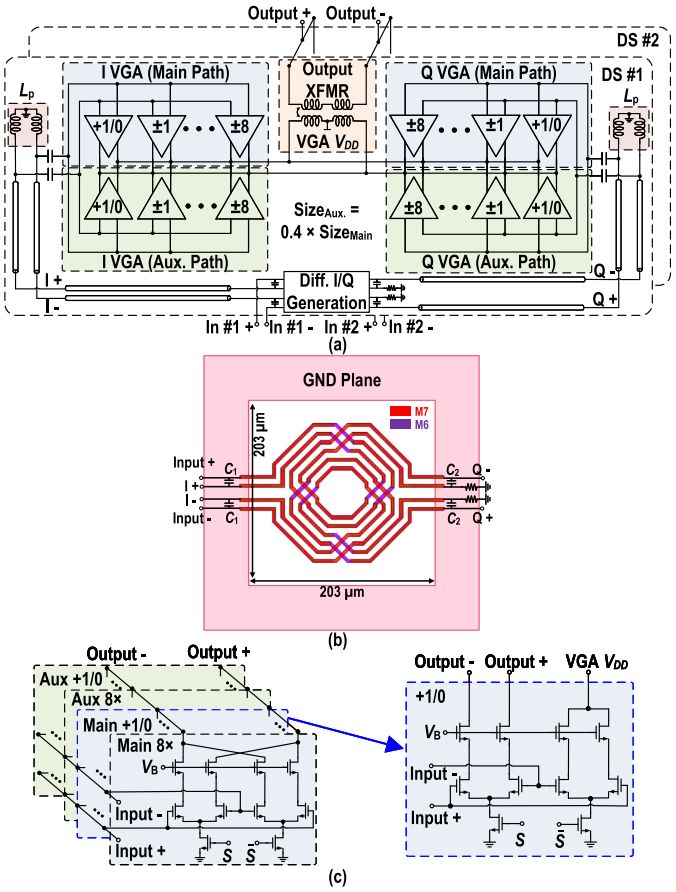

Fig. 14. (a) VM schematic including the main path and auxiliary path. (b) EM model of the folded-transformer-based I/Q generation network. (c) Schematic of the digitally controlled VGA cells.

output, represented as $V_{ij}(\angle\beta_{ij} + \xi_{ij}\angle\alpha_{ij})$, is subsequently amplified by a power amplifier (PA).

A. Main-Path and Auxiliary-Path Vector Modulators

The schematic of 5-bit main-path and auxiliary-path VMs is shown in Fig. 14(a). The input RF signal is first split into differential in-phase (I) and quadrature (Q) signals using a folded-transformer-based I/Q generation network [38] [see Fig. 14(b)], which offers magnetic field enhancement for size reduction (203 × 203 μm). Capacitors C_1 and C_2 are used to minimize the amplitude and phase mismatches between the I and Q signals. The I/Q outputs are then routed to I/Q VGAs through 100-Ω differential transmission lines (T-Lines).

The phase shifting is achieved by adjusting the current weighting of I/Q VGAs. As shown in Fig. 14(c), each VGA includes four binary-weighted cells (±1 to ±8) and a half-bit (+1/0), offering a normalized gain from "−15" to "+16" [39]. These VGA cells are designed as differential cascode amplifiers controlled by tail switches. When the control signal S is high (or low), the left (or right) branch of the VGA cell is turned on, yielding a "+" (or "−") output current. One advantage of this topology is that both the VGA input and output are always loaded by one "ON" and one "OFF" differential pair regardless of the VGA weighting, ensuring a constant input and output capacitance. The input capacitance

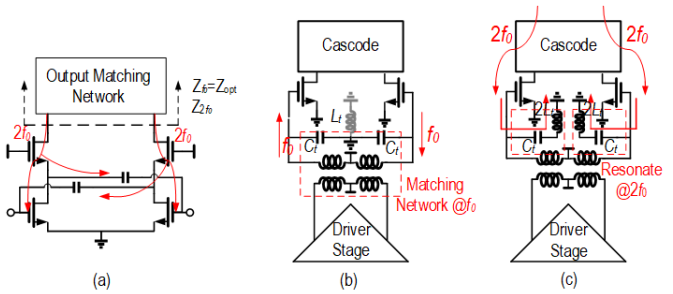

Fig. 15. (a) Second harmonic feedback from drain to gate. A second harmonic trap is added at the gate to enhance linearity. (b) and (c) Equivalent circuits at the fundamental frequency and second harmonic, respectively.

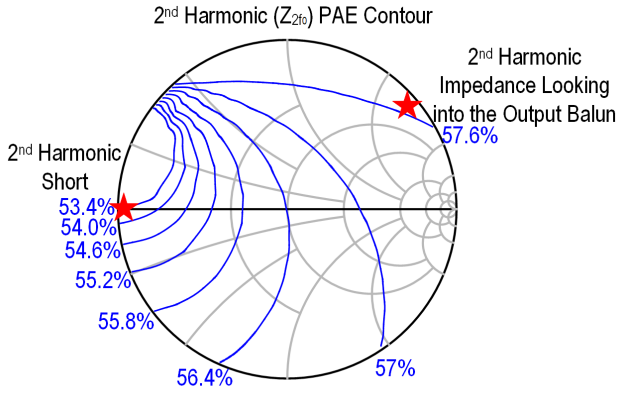

Fig. 16. Second harmonic loadpull simulation for the cascode output stage. Although a second harmonic short at the PA output can improve the PA linearity, it may compromise the efficiency.

is resonated out by a differential inductor L_p. The output capacitance is absorbed into the output transformer design. The transformer outputs of the two DSs are current summed and further amplified by a three-stage PA.

As mentioned in Section III-A, the amplitude scaling factor of the auxiliary path is designed to be 0.4× for notch steering. Since differential I and Q signals are readily available from the main-path VM, this amplitude scaling is achieved by reducing the size of auxiliary-path VGA cells [see Fig. 14(a)]. Considering that the VGA cells are designed only using transistors, the chip area overhead introduced by the auxiliary-path VM is kept minimal.

B. Three-Stage Power Amplifier

For a hybrid beamforming TX with multiple independent DSs, the linearity and efficiency of the PA are particularly important [40]. In terms of linearity, it is known that the second harmonic at the output drain terminal can feedback to the gate and then mix with the fundamental tone, generating IM3 distortions and thereby degrading the PA linearity [41]. This mechanism is conceptually illustrated in Fig. 15(a). Recent research has shown that adding a second harmonic trap at the drain, which provides a low-impedance path for the second harmonic, can improve the PA linearity [42], [43]. However, as PA efficiency is sensitive to harmonic terminations, having a second harmonic short at the PA output may compromise its efficiency. To illustrate this, we perform a second harmonic loadpull simulation for our cascode output stage, as shown in Fig. 16. The simulation result indicates that our PA actually prefers a high second harmonic impedance to achieve a Class F^{-1}-like output voltage waveform for better efficiency.

To filter out the second harmonic while keeping high efficiency, we introduce a second harmonic trap at the gate. Additionally, the output balun is designed to realize a high impedance at the second harmonic along with the desired optimal impedance at the fundamental frequency (see Fig. 16). The second harmonic trap consists of an inductor L_t and two capacitors C_t. At the fundamental frequency, L_t is shorted to the ground, and two C_t are incorporated into the matching network design [see Fig. 15(b)]. At the second harmonic, C_t and $2L_t$ form a series LC resonance [see Fig. 15(c)], creating a second harmonic trap. The inductor L_t is implemented using two shunt inductors in parallel to maintain symmetry.

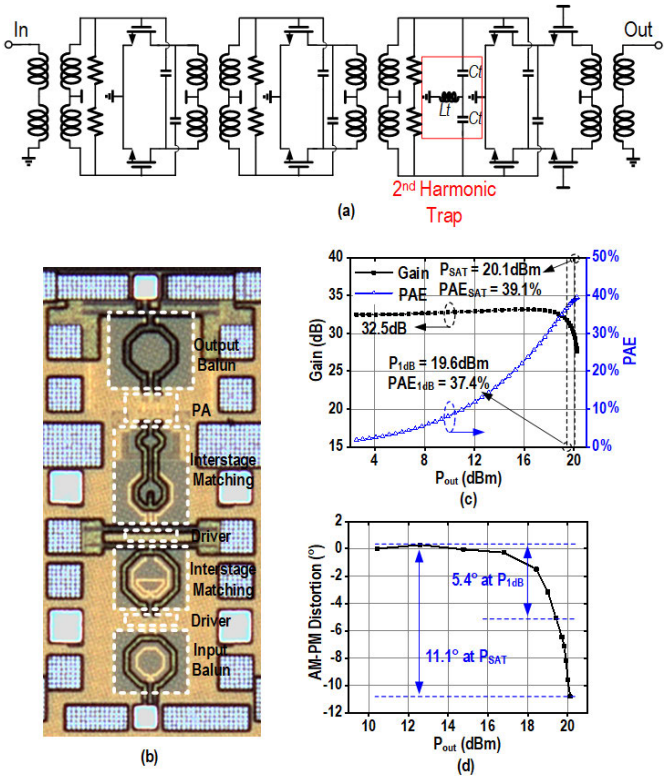

Fig. 17. PA standalone test structure. (a) Schematic, (b) die micrograph, and (c) and (d) large-signal continuous-wave measurement results at 28 GHz.

A compact footprint of 44 × 44 μm is achieved through a three-turn coil design.

The complete schematic of the three-stage PA is shown in Fig. 17(a), consisting of a cascode output stage and two common-source driver stages. To characterize its performance, we implement a standalone PA test structure, with its chip micrograph shown in Fig. 17(b). At the center frequency of 28 GHz, it achieves 32.5-dB power gain, 19.6-dBm output 1-dB compression point ($P_{1\,\mathrm{dB}}$), 20.1-dBm output saturated power (P_{SAT}), and 37.4%/39.1% power-added-efficiency (PAE) at $P_{1\,\mathrm{dB}}/P_{\mathrm{SAT}}$ [see Fig. 17(c)]. The measured AM-PM distortions are 5.4° and 11.1° at $P_{1\,\mathrm{dB}}$ and P_{SAT}, respectively [see Fig. 17(d)]. These performance metrics demonstrate state-of-the-art linearity and efficiency compared with recently

TABLE I
PERFORMANCE COMPARISON WITH RECENTLY REPORTED 28-GHz PAs IN ANTENNA-ARRAY DEMONSTRATIONS

	This Work	JSSC 2021 [36]	JSSC 2017 [44]	JSSC 2020 [45]	TMTT 2021 [46]	JSSC 2022 [47]	JSSC 2022 [48]
Freq. (GHz)	28	28	28	28	24-28	28	27
P_{SAT} (dBm)	**20.1**	16.6*	16	16.1*	18.4*	17.4	18.8
PAE_{SAT}	**39.1%**	34.6%*	20.5%	21.4%*	N/A	38.8%[b]	30.1%
P_{1dB} (dBm)	**19.6**	14.2*	13.5	14.4*	16.3*	15[ab]	17.5
PAE_{1dB}	**37.4%**	N/A	N/A	16.1%*	25.2%*	32%[ab]	29.5%[b]
Technology	45-nm CMOS SOI	65-nm CMOS	130-nm SiGe	65-nm CMOS	65-nm CMOS	45-nm CMOS SOI	28-nm CMOS

* T/R switch loss deembeded. [a] Graphically estimated. [b] Drain efficiency including PA and driver.

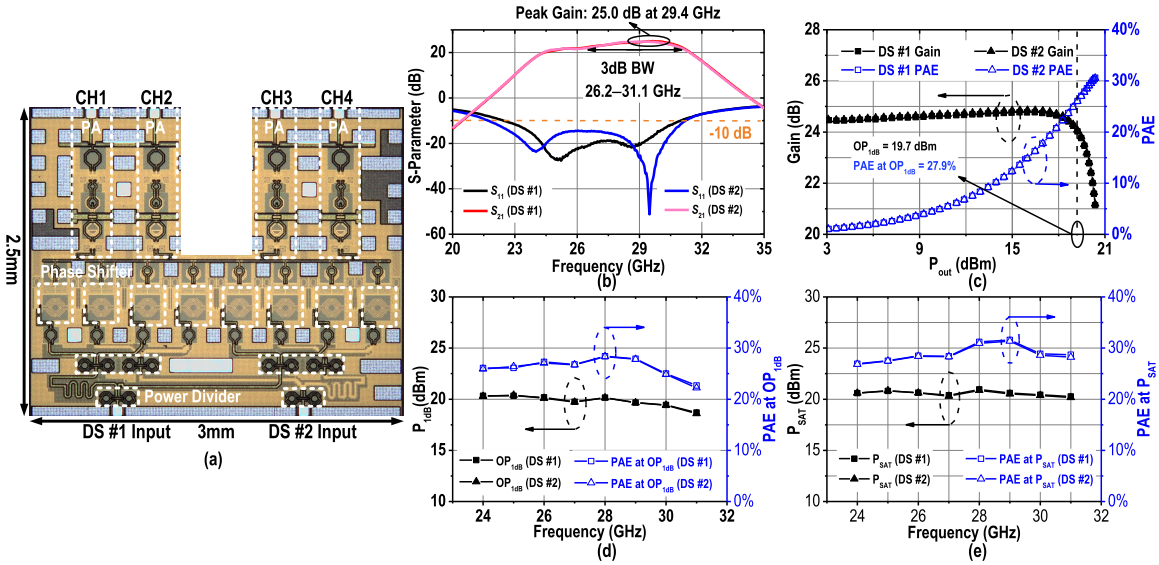

Fig. 18. (a) Chip micrograph of the four-element FC hybrid beamformer. (b) S-parameters measurement results. (c) Single-channel large-signal measurement at 29 GHz. (d) Single-channel $P_{1\,dB}$ versus frequency. (e) Single-channel P_{SAT} versus frequency.

reported 28-GHz PAs that are integrated into antenna arrays (see Table I).

V. MEASUREMENT RESULTS

The TX prototype is implemented in the GlobalFoundries 45-nm CMOS SOI process. The chip micrograph is shown in Fig. 18(a). This section presents our measurement results based on probing and OTA tests.

A. Probing-Based Measurement Results

The measured S-parameters from the chip input to the channel output are shown in Fig. 18(b). The power gains of the two DSs are well-matched, achieving a 3-dB bandwidth from 26.2 to 31.1 GHz and a peak gain of 25.0 dB at 29.4 GHz. Large-signal power sweep at 29 GHz and large-signal frequency sweep are shown in Fig. 18(c)–(e). The two DSs present almost identical large-signal performance, achieving 19.7-dBm $OP_{1\,dB}$, 20.4-dBm P_{SAT}, 27.9% PAE at $OP_{1\,dB}$, and 30.6% peak PAE at 29 GHz, which demonstrates state-of-the-art TX output power, efficiency, and linearity. From 24 to 31 GHz, the two DSs achieve >18.6/20.1-dBm $OP_{1\,dB}/P_{SAT}$ with >22.2%/26.5% PAE at $OP_{1\,dB}/P_{SAT}$.

Next, we characterize the phase-shifting performance of main-path and auxiliary-path VMs using the setup shown in Fig. 19(a). When measuring the main-path (or the auxiliary-path) I/Q constellation, the gain of the other path is set to be zero. In the measurement, the I/Q VGA control code is incremented from 0 to 31 to generate I/Q VGA output weights from "−15" to "+16," resulting in a total of 1024 I/Q constellation points. As shown in Fig. 19(b)–(d), 120 out of 146 points are selected within the 1-dB ring to steer the main beam, achieving a 3° phase shift resolution, a 0.96° root-mean-square (rms) phase error, and a 0.28-dB rms amplitude error at 29 GHz. The measured rms phase and amplitude errors remain consistent from 24 to 31 GHz. The measured constellations of the main-path and auxiliary-path VMs for all four channels are shown in Fig. 20, demonstrating great consistency. The output power in these measurements is set to be 9-dB back-off from $OP_{1\,dB}$, which resembles the averaged output power of amplifying two independent single-carrier (SC) 16-/64-QAM signals each with ∼6-dB peak-to-average power ratio (PAPR).

From the measured I/Q constellations, the main-path and auxiliary-path VMs settings can be determined based on (8) and (9), respectively. After selecting the desired settings, we program the chip, probe the outputs of the four channels sequentially, and synthesize the AF in MATLAB. When the main beam is fixed at 0° and the spatial notch is steered from ±22° to ±90° (i.e., outside the −10-dB beamwidth of

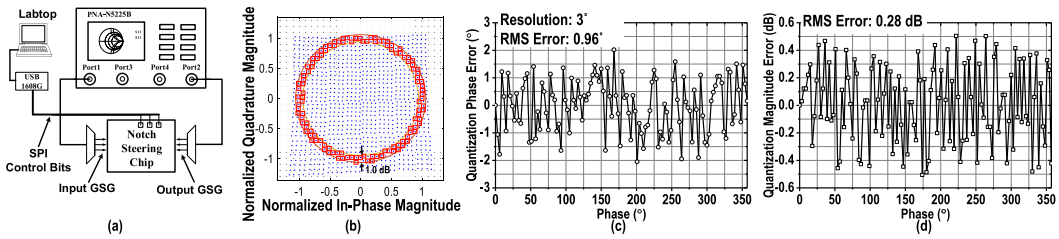

Fig. 19. (a) VM constellation measurement setup. (b) Measured main-path VM constellation with 9-dB PBO from $OP_{1\,dB}$ at 29 GHz. (c) Measured main-path VM phase quantization error and (d) magnitude quantization error at 29 GHz.

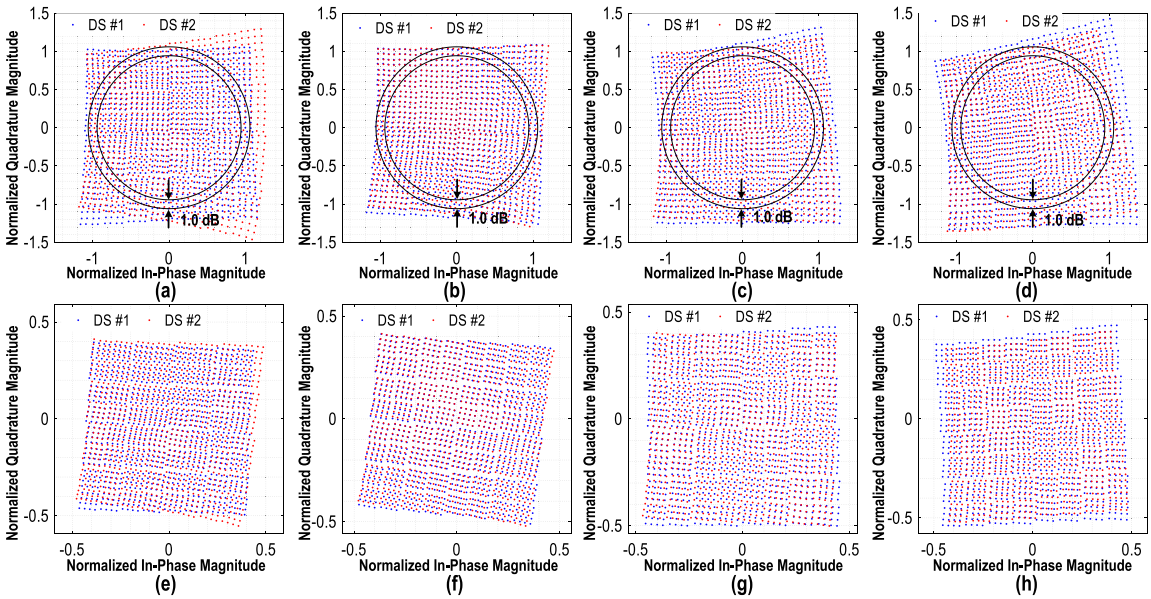

Fig. 20. (a)–(d) Measured constellations for the four main-path VMs. (e)–(h) Measured constellations for the four auxiliary-path VMs. All measurements are performed at 9-dB back-off from $OP_{1\,dB}$ at 29 GHz.

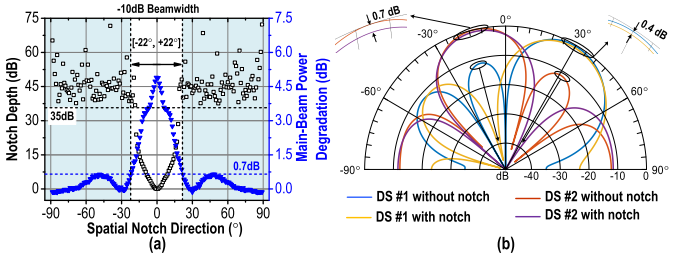

Fig. 21. (a) Notch depth and main-beam power degradation versus notch angles. (b) Demo showing the sidelobes are rejected for both DSs.

the main beam) with 1° per step, the achieved notch depth is >35 dB, and the main-beam power degradation remains <0.7 dB, as shown in Fig. 21(a). Additionally, a two-DS notch steering demonstration is shown in Fig. 21(b). The main beams of DS #1 and #2 are pointed toward 30° and −13°, respectively. In this case, the sidelobe of one DS is aligned with the main beam of the other DS. By enabling the auxiliary-path VM, deep notches of >45 dB are synthesized in the two sidelobe directions with <0.7 dB of main-beam power degradation for both DSs.

B. OTA CW Measurement Results

The TX chip is wire-bonded to a printed circuit board (PCB) and interfaced with a four-element $\lambda/2$-spaced dipole antenna array for OTA measurements, as shown in Fig. 22(a). The PCB is designed using a two-layer Rogers RT/duroid 5880 substrate.

The antenna pattern measurements are performed inside an antenna chamber. As shown in Fig. 22(b), the separation between the packaged TX and the RX horn antenna is 0.5 m, resulting in a free-space path loss (FSPL) of 55 dB at 29 GHz. Before enabling the notch steering, we first measure the array scanning performance. Fig. 22(c) presents the measured beam pattern when the main beam is steered from −45° to 45°. When the main beam is steered toward 0°, the measured 3-dB beamwidth is 26°. The measured equivalent isotropic radiated power (EIRP) at the 1-dB compression point ($EIRP_{1\,dB}$) is 29.8 dBm.

Next, we set the main beam to be 0° for DS #1 and steer the notch toward the sidelobe. As shown in Fig. 23(a), before enabling the notch, the sidelobe level is −12.1 dB at −47° (indicated by the blue line). Upon activating the auxiliary path, a notch depth of 41.9 dB and a main-beam power degradation of 0.34 dB are achieved. Fig. 23(b) presents the beam pattern measurements for two DSs. The main beams of DS #1 and DS #2 are pointed toward −13° and 30°, respectively. Under this scenario, the sidelobe of DS #1 coincides with the main lobe of DS #2 and vice versa. After enabling the auxiliary-path VM, the achieved notch depths are 37.8 and 30.2 dB, respectively, for the two DSs.

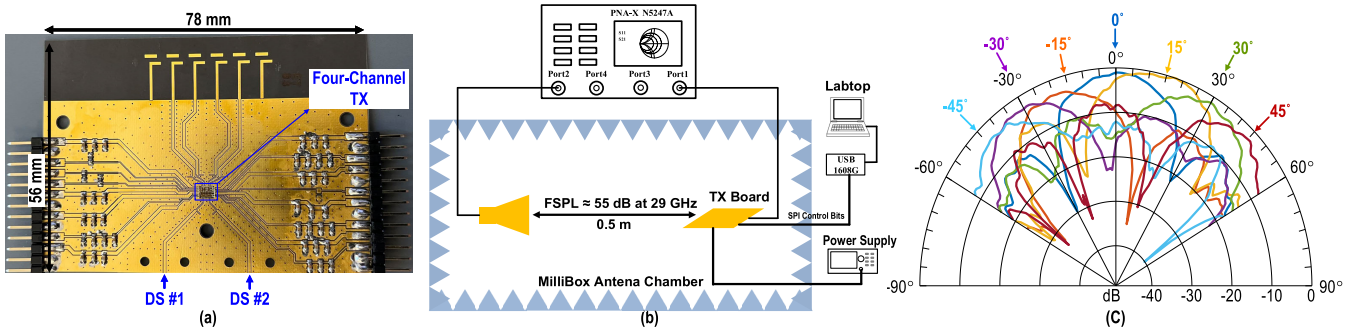

Fig. 22. (a) TX chip packaged with on-board dipole antennas. (b) OTA measurement setup. (c) Measured beam patterns.

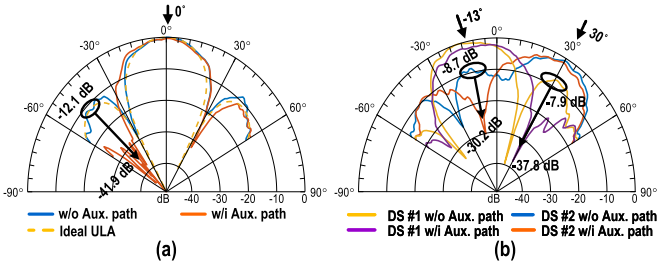

Fig. 23. (a) Measured patterns with the auxiliary-path VMs enabled to cancel the sidelobe. (b) Measured patterns to steer two spatial notches for the two DSs.

Notch Location	-50°	-45°	-40°	-35°	-30°	-25°	25°	30°	35°	40°	45°	50°
Main Beam Degradation (dB)	0.65	0.34	0.06	0	0.31	0.78	0.43	0.24	0.63	0.37	0.55	0.60
Notch Depth (dB)	38.4	41.9	39.1	39.0	33.4	35.0	36.7	36.6	50.5	39.6	41.8	37.7

(a)

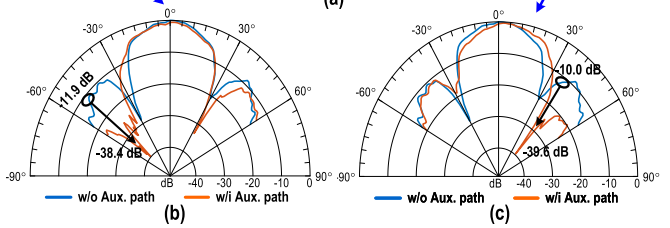

Fig. 24. (a) Measured notch depth and main-beam power degradation with the main beam fixed at 0° and the notch swept across different angles. Measured beam patterns when the notch is positioned at (b) −50° and (c) 40°.

We also steer the notch outside the −10-dB beamwidth from ±50° to ±25° with an increment of 5°. The corresponding notch depths and main-beam degradation are shown in Fig. 24. Except at −30°, the achieved notch depth consistently exceeds 35 dB. It is also important to note that the main-beam power degradation remains <0.8 dB during notch steering. These measurement results closely align with our simulations presented in Section III and probing-based measurement results in Section V-A, demonstrating the robustness of our proposed notch steering scheme.

C. OTA Modulation Measurement Results

Finally, we perform two OTA modulation demonstrations. The received signal at the far-field is picked up by a horn antenna and monitored using a spectrum analyzer.

In the first demonstration [see Fig. 25(a)–(d)], DS #1 transmits a 400-MSym/s SC 64-QAM modulated signal at 29 GHz toward 0°. Meanwhile, DS #2 sends out a 29-GHz CW signal toward 45° with its sidelobe pointing to 0°, thus serving as a strong co-channel interference for DS #1. The integrated power of DS #1 and #2 are both set to be 9-dB back-off from $OP_{1\,dB}$.

When only DS #1 is turned on, the measured error vector magnitude (EVM) is −30.4 dB with an EIRP of 20.8 dBm [see Fig. 25(a)]. After turning on DS #2 but without enabling the spatial notch, DS #1 cannot be demodulated due to the insufficient SINR of 11.5 dB [see Fig. 25(b)]. Then, we enable the auxiliary path of DS #2 to steer a spatial notch toward 0°. DS #1 can now be successfully demodulated with an EVM of −28.9 dB and an EIRP of 20.6 dBm [see Fig. 25(c)]. Compared to the case without DS #2 [see Fig. 25(a)], the EVM is degraded by 1.5 dB. This EVM degradation is due to two reasons. First, the PA operates in the higher power region after enabling DS #2, close to 6-dB back-off from $OP_{1\,dB}$, which results in compromised linearity. Second, there still exists a weak residue interference caused by DS #2 because of the finite notch depth. To characterize how much attenuation is achieved for the interference, we disable DS #1 and compare the signal strengths before and after enabling the spatial notch [see Fig. 25(b) and (d)]. The interference is attenuated by 23.7 dB, which is equivalent to a notch depth of 35.2 dB. This demonstration is repeated with increased TX power, achieving an EVM of −25.2 dB at 22.0-dBm EIRP when enabling notch steering for DS #2.

In the second demonstration, we apply the same 400-MSym/s SC 64-QAM modulation for DS #2 to show the notch steering performance for a wideband co-channel interference. To be able to distinguish between DS #1 and #2 on the spectrum analyzer, we offset their center frequency by 200 MHz.

As shown in Fig. 25(e)–(h), after enabling the spatial notch for DS #2 at 0°, the measured EVM for DS #1 is −28.2 dB, slightly lower than that in the first demonstration with a CW interference [see Fig. 25(c)]. Nevertheless, this measurement demonstrates that our proposed notch steering scheme is capable of suppressing wideband interference whose bandwidths are comparable to the channel bandwidth of 5G NR signals. Additionally, it demonstrates that our hybrid beamforming

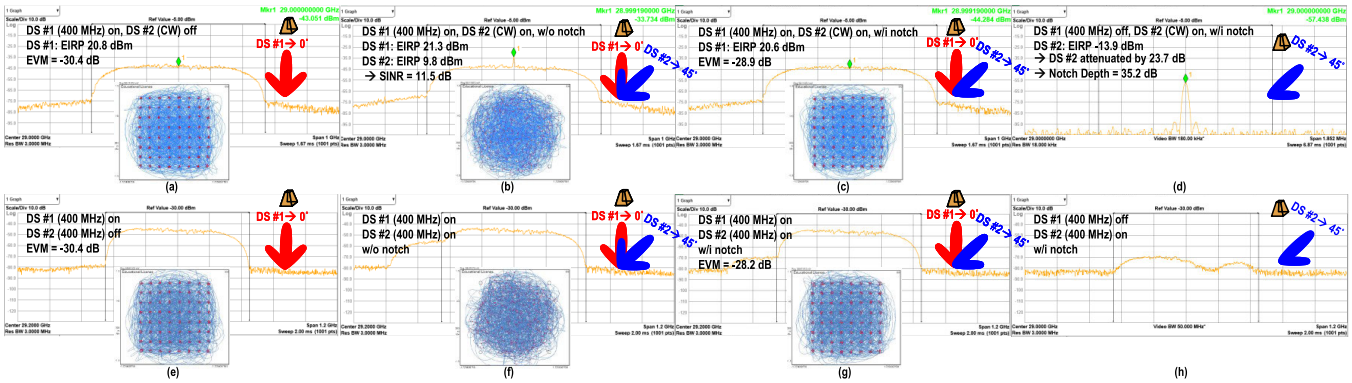

Fig. 25. (a) DS #1 transmits a 400-MSym/s 64-QAM signal toward 0°, yielding an EIRP of 20.8 dBm and an EVM of −30.4 dB. (b) After turning on DS #2, which is a CW interference whose sidelobe aligns with the main lobe of DS #1, DS #1 cannot be demodulated due to insufficient SINR. (c) After enabling notch steering, DS #1 can be demodulated again with an EIRP of 20.6 dBm and an EVM of −28.9 dB. (d) Disabling DS #1 to illustrate the attenuation of DS #2 by the notch steering. (e)–(h) Repeat the OTA demonstration but apply a 400-MSym/s 64-QAM signal for DS #2. Center frequency of DS #1 is offset by 200 MHz so we can distinguish DS #1 and DS #2 on the spectrum analyzer.

TABLE II
PERFORMANCE COMPARISON WITH STATE-OF-THE-ART 28-GHz TXs SUPPORTING DUAL DSs

Reference	This Work	JSSC'22 [9]	JSSC'22 [28]	JSSC'21 [36]
Beamforming Architecture	**Hybrid (Fully Connected)**	Hybrid (Fully Connected)	Analog	Analog
Frequency (GHz)	**29**	28/37	24–30	28
# of Elements / Chip	**4 TX**	8 TRX	2 × 8 TRX	2 × 4 TRX
Phase Resolution (°)	**3.0**	N/A	4–5.6	N/A
RMS Gain Error (dB)	**0.28**	N/A	±0.5	0.12
RMS Phase Error (°)	**0.96**	N/A	1.35	0.4
P_{SAT} (dBm) / Element	**20.4**	15.5	17	16.1
OP_{1dB} (dBm) / Element	**19.7**	14	16	13.7
TX Efficiency / Element	**27.8% (at P_{1dB}) 30.6% (at P_{SAT})**	15.5%**(at P_{1dB}) 21%**(at P_{SAT})	22.1%* (at P_{1dB}) 23.3%* (at P_{SAT})	21.9%* (at P_{SAT})
Number of Data Streams	**2 (Same Polarization)**	2 (Same Polarization)	2 (Dual Polarization)	2 (Dual Polarization)
Modulation Scheme	**64-QAM**	16-QAM	64-QAM OFDM	64-QAM OFDMA
Notch Steering	**Yes (Notch Depth >35 dB)**	Yes (Notch Depth >25 dB)	No	No
Modulation Bandwidth (MHz)	**400**	250	400	400
TX EVM (dB)	**–28.9 / –25.2 (9.2- / 7.8-dB PBO from $EIRP_{1dB}$ per DS with CW Interference)**	–24.8 (12.5-dB PBO from OP_{1dB} per DS)	–32.1	–25.8 (9.4-dB PBO from $EIRP_{SAT}$)
Chip Area (mm^2)	**7.5**	12.65	36.96	16
Technology	**45-nm CMOS SOI**	65-nm CMOS	130-nm SiGe BiCMOS	65-nm CMOS

*Efficiency calculated based on reported output power and DC power consumption. **PA PAE.

TX is able to support two concurrent, independent DSs toward two spatial directions at the same frequency.

VI. CONCLUSION

This article presents a notch steering scheme that leverages a set of auxiliary-path VMs to form an interference-canceling beam. By spatially combining the AFs of the main beam and the interference-canceling beam, a deep spatial notch is created with minimal main-beam power degradation. Unlike the conventional zero-forcing method that requires matrix inversion in digital for spatial notch creation, our scheme enables the computation of antenna weights in analog, significantly reducing the computational cost and latency.

Leveraging this new notch steering technique, a 28-GHz four-element FC hybrid beaming TX is demonstrated. It is capable of concurrently transmitting two independent DSs with a high SINR and a low main-beam power degradation. In probing-based measurements, each TX channel delivers 19.7-dBm $OP_{1\,dB}$, 20.4-dBm P_{SAT}, and 30.6% peak PAE at 29 GHz, demonstrating state-of-the-art TX linearity and efficiency performance. In OTA measurements, it achieves 29.8-dBm $EIRP_{1\,dB}$ and is able to steer a spatial notch outside the −10-dB beamwidth of the main beam, with a notch depth of >35 dB and a main-beam power degradation of <0.8 dB. Moreover, the packaged TX module demonstrates an EVM of −25.2 dB for a 400-MHz 64-QAM signal with an EIRP of 22.0 dBm, while creating a spatial notch for the other DS.

A performance comparison with recently reported 28-GHz TXs that can support dual DSs is summarized in Table II. In addition to demonstrating the highest single-channel output power and efficiency, this work is capable of simultaneously supporting two independent, wideband modulated DSs in

the same polarization through the proposed notch steering scheme. The proposed scheme may find wide applications in hybrid beamforming arrays to support spatial multiplexing for SU-MIMO and MU-MIMO systems.

ACKNOWLEDGMENT

The authors would like to thank GlobalFoundries for chip fabrication, and Keysight and Rohde & Schwarz for measurement equipment support. They also thank the members of the Rice Integrated Systems and Electromagnetics (RISE) Laboratory for their valuable technical discussions and continued support throughout this project.

REFERENCES

[1] S. Han, C.-L. I, Z. Xu, and C. Rowell, "Large-scale antenna systems with hybrid analog and digital beamforming for millimeter wave 5G," *IEEE Commun. Mag.*, vol. 53, no. 1, pp. 186–194, Jan. 2015.

[2] Q. Xue, X. Fang, and C.-X. Wang, "Beamspace SU-MIMO for future millimeter wave wireless communications," *IEEE J. Sel. Areas Commun.*, vol. 35, no. 7, pp. 1564–1575, Jul. 2017.

[3] J. Pang et al., "A 28-GHz CMOS phased-array beamformer utilizing neutralized bi-directional technique supporting dual-polarized MIMO for 5G NR," *IEEE J. Solid-State Circuits*, vol. 55, no. 9, pp. 2371–2386, Sep. 2020.

[4] B. Yang, Z. Yu, J. Lan, R. Zhang, J. Zhou, and W. Hong, "Digital beamforming-based massive MIMO transceiver for 5G millimeter-wave communications," *IEEE Trans. Microw. Theory Techn.*, vol. 66, no. 7, pp. 3403–3418, Jul. 2018.

[5] Y.-S. Yeh and B. A. Floyd, "Multibeam phased-arrays using dual-vector distributed beamforming: Architecture overview and 28 GHz transceiver prototypes," *IEEE Trans. Circuits Syst. I, Reg. Papers*, vol. 67, no. 12, pp. 5496–5509, Dec. 2020.

[6] E. Naviasky, L. Iotti, G. LaCaille, B. Nikolic, E. Alon, and A. M. Niknejad, "A 71-to-86-GHz 16-element by 16-beam multi-user beamforming integrated receiver sub-array for massive MIMO," *IEEE J. Solid-State Circuits*, vol. 56, no. 12, pp. 3811–3826, Dec. 2021.

[7] S. Mondal, R. Singh, A. I. Hussein, and J. Paramesh, "A 25–30 GHz fully-connected hybrid beamforming receiver for MIMO communication," *IEEE J. Solid-State Circuits*, vol. 53, no. 5, pp. 1275–1287, May 2018.

[8] S. Mondal and J. Paramesh, "A reconfigurable 28-/37-GHz MMSE-adaptive hybrid-beamforming receiver for carrier aggregation and multi-standard MIMO communication," *IEEE J. Solid-State Circuits*, vol. 54, no. 5, pp. 1391–1406, May 2019.

[9] S. Mondal, L. R. Carley, and J. Paramesh, "Dual-band, two-layer millimeter-wave transceiver for hybrid MIMO systems," *IEEE J. Solid-State Circuits*, vol. 57, no. 2, pp. 339–355, Feb. 2022.

[10] P. Heydari, "Terahertz integrated circuits and systems for high-speed wireless communications: Challenges and design perspectives," *IEEE Open J. Solid-State Circuits Soc.*, vol. 1, pp. 18–36, 2021.

[11] H. Mohammadnezhad, R. Abedi, and P. Heydari, "A millimeter-wave partially overlapped beamforming-MIMO receiver: Theory, design, and implementation," *IEEE Trans. Microw. Theory Techn.*, vol. 67, no. 5, pp. 1924–1936, May 2019.

[12] N. Li et al., "A four-element 7.5–9-GHz phased-array receiver with 1–8 simultaneously reconfigurable beams in 65-nm CMOS," *IEEE Trans. Microw. Theory Techn.*, vol. 69, no. 1, pp. 1114–1126, Jan. 2021.

[13] M. Huang, T. Chi, F. Wang, T. Li, and H. Wang, "A full-FoV autonomous hybrid beamformer array with unknown blockers rejection and signals tracking for low-latency 5G mm-wave links," *IEEE Trans. Microw. Theory Techn.*, vol. 67, no. 7, pp. 2964–2974, Jul. 2019.

[14] M.-Y. Huang, T. Chi, F. Wang, T.-W. Li, and H. Wang, "A 23-to-30 GHz hybrid beamforming MIMO receiver array with closed-loop multistage front-end beamformers for full-FoV dynamic and autonomous unknown signal tracking and blocker rejection," in *IEEE Int. Solid-State Circuits Conf. (ISSCC) Dig. Tech. Papers*, Feb. 2018, pp. 68–70.

[15] S. A. Schelkunoff, "A mathematical theory of linear arrays," *Bell Syst. Tech. J.*, vol. 22, no. 1, pp. 80–107, Jan. 1943.

[16] C. A. Balanis, *Antenna Theory: Analysis and Design*. Hoboken, NJ, USA: Wiley, 2005.

[17] H. M. Ibrahim, "Null steering by real-weight control—A method of decoupling the weights," *IEEE Trans. Antennas Propag.*, vol. 39, no. 11, pp. 1648–1650, Nov. 1991.

[18] S. Mehmood, Z. U. Khan, F. Zaman, and B. Shoaib, "Performance analysis of the different null steering techniques in the field of adaptive beamforming," *Res. J. Appl. Sci., Eng. Technol.*, vol. 5, no. 15, pp. 4006–4012, Apr. 2013.

[19] D. Davies, "Independent angular steering of each zero of the directional pattern for a linear array," *IEEE Trans. Antennas Propag.*, vol. AP-15, no. 2, pp. 296–298, Mar. 1967.

[20] H. Steyskal, "Simple method for pattern nulling by phase perturbation," *IEEE Trans. Antennas Propag.*, vol. AP-31, no. 1, pp. 163–166, Jan. 1983.

[21] P. J. Kajenski, "Phase only antenna pattern notching via a semidefinite programming relaxation," *IEEE Trans. Antennas Propag.*, vol. 60, no. 5, pp. 2562–2565, May 2012.

[22] H. Steyskal, R. Shore, and R. Haupt, "Methods for null control and their effects on the radiation pattern," *IEEE Trans. Antennas Propag.*, vol. AP-34, no. 3, pp. 404–409, Mar. 1986.

[23] B. D. Van Veen and K. M. Buckley, "Beamforming: A versatile approach to spatial filtering," *IEEE ASSP Mag.*, vol. ASSP-5, no. 2, pp. 4–24, Apr. 1988.

[24] M. Chryssomallis, "Smart antennas," *IEEE Antennas Propag. Mag.*, vol. 42, no. 3, pp. 129–136, Jun. 2000.

[25] Y. Aslan, A. Roederer, N. J. G. Fonseca, P. Angeletti, and A. Yarovoy, "Orthogonal versus zero-forced beamforming in multibeam antenna systems: Review and challenges for future wireless networks," *IEEE J. Microw.*, vol. 1, no. 4, pp. 879–901, Oct. 2021.

[26] A. Puglielli et al., "Design of energy- and cost-efficient massive MIMO arrays," *Proc. IEEE*, vol. 104, no. 3, pp. 586–606, Mar. 2016.

[27] B. Sadhu et al., "A 24-to-30 GHz 256-element dual-polarized 5G phased array with fast beam-switching support for >30,000 beams," in *IEEE Int. Solid-State Circuits Conf. (ISSCC) Dig. Tech. Papers*, vol. 65, Feb. 2022, pp. 436–438.

[28] B. Sadhu et al., "A 24–30-GHz 256-element dual-polarized 5G phased array using fast on-chip beam calculators and magnetoelectric dipole antennas," *IEEE J. Solid-State Circuits*, vol. 57, no. 12, pp. 3599–3616, Dec. 2022.

[29] Y. Hu, X. Zhang, and T. Chi, "A 28 GHz hybrid-beamforming transmitter array supporting concurrent dual data steams and spatial notch steering for 5G MIMO," in *Proc. IEEE Custom Integr. Circuits Conf. (CICC)*, Apr. 2021, pp. 1–2.

[30] K. Kibaroglu, M. Sayginer, T. Phelps, and G. M. Rebeiz, "A 64-element 28-GHz phased-array transceiver with 52-dBm EIRP and 8–12-Gb/s 5G link at 300 meters without any calibration," *IEEE Trans. Microw. Theory Techn.*, vol. 66, no. 12, pp. 5796–5811, Dec. 2018.

[31] Y. Yoon et al., "A highly linear 28GHz 16-element phased-array receiver with wide gain control for 5G NR application," in *Proc. IEEE Radio Freq. Integr. Circuits Symp. (RFIC)*, Jun. 2019, pp. 287–290.

[32] J. Park, S. Lee, J. Chun, L. Jeon, and S. Hong, "A 28-GHz four-channel beamforming front-end IC with dual-vector variable gain phase shifters for 64-element phased array antenna module," *IEEE J. Solid-State Circuits*, vol. 58, no. 4, pp. 1142–1159, Apr. 2023.

[33] Y. Yi et al., "A 24–29.5-GHz highly linear phased-array transceiver front-end in 65-nm CMOS supporting 800-MHz 64-QAM and 400-MHz 256-QAM for 5G new radio," *IEEE J. Solid-State Circuits*, vol. 57, no. 9, pp. 2702–2718, Sep. 2022.

[34] K. Kibaroglu, M. Sayginer, and G. M. Rebeiz, "A low-cost scalable 32-element 28-GHz phased array transceiver for 5G communication links based on a 2×2 beamformer flip-chip unit cell," *IEEE J. Solid-State Circuits*, vol. 53, no. 5, pp. 1260–1274, May 2018.

[35] T. Chi, J. Park, S. Li, and H. Wang, "A millimeter-wave polarization-division-duplex transceiver front-end with an on-chip multifeed self-interference-canceling antenna and an all-passive reconfigurable canceller," *IEEE J. Solid-State Circuits*, vol. 53, no. 12, pp. 3628–3639, Dec. 2018.

[36] J. Pang et al., "A CMOS dual-polarized phased-array beamformer utilizing cross-polarization leakage cancellation for 5G MIMO systems," *IEEE J. Solid-State Circuits*, vol. 56, no. 4, pp. 1310–1326, Apr. 2021.

[37] T. Chi, J. S. Park, S. Li, and H. Wang, "A 64 GHz full-duplex transceiver front-end with an on-chip multifeed self-interference-canceling antenna and an all-passive canceler supporting 4 Gb/s modulation in one antenna footprint," in *IEEE Int. Solid-State Circuits Conf. (ISSCC) Dig. Tech. Papers*, Feb. 2018, pp. 76–78.

[38] J. S. Park and H. Wang, "A K-band 5-bit digital linear phase rotator with folded transformer based ultra-compact quadrature generation," in *Proc. IEEE Radio Freq. Integr. Circuits Symp.*, Jun. 2014, pp. 75–78.

[39] S. Dong et al., "A 140 GHz RF beamforming phased-array receiver supporting >20 dB IRR with 8 GHz channel bandwidth at low IF in 22 nm FDSOI CMOS," in *Proc. IEEE Radio Freq. Integr. Circuits Symp. (RFIC)*, Jun. 2023, pp. 293–296.

[40] X. Zhang, S. Li, D. Huang, and T. Chi, "A millimeter-wave three-way Doherty power amplifier for 5G NR OFDM," *IEEE J. Solid-State Circuits*, vol. 58, no. 5, pp. 1256–1270, May 2023.

[41] B. Park et al., "Highly linear mm-wave CMOS power amplifier," *IEEE Trans. Microw. Theory Techn.*, vol. 64, no. 12, pp. 4535–4544, Dec. 2016.

[42] D. Jeong et al., "Linear CMOS power amplifier at Ka-band with ultra-wide video bandwidth," in *Proc. IEEE Radio Freq. Integr. Circuits Symp. (RFIC)*, Jun. 2017, pp. 220–223.

[43] H.-C. Park et al., "A high efficiency 39 GHz CMOS cascode power amplifier for 5G applications," in *Proc. IEEE Radio Freq. Integr. Circuits Symp. (RFIC)*, Jun. 2019, pp. 179–182.

[44] B. Sadhu et al., "A 28-GHz 32-element TRX phased-array IC with concurrent dual-polarized operation and orthogonal phase and gain control for 5G communications," *IEEE J. Solid-State Circuits*, vol. 52, no. 12, pp. 3373–3391, Dec. 2017.

[45] S. Mondal and J. Paramesh, "Power-efficient design techniques for mm-wave hybrid/digital FDD/full-duplex MIMO transceivers," *IEEE J. Solid-State Circuits*, vol. 55, no. 8, pp. 2011–2026, Aug. 2020.

[46] W. Zhu et al., "A 24–28-GHz four-element phased-array transceiver front end with 21.1%/16.6% transmitter peak/OP1dB PAE and sub-degree phase resolution supporting 2.4 Gb/s in 256-QAM for 5-G communications," *IEEE Trans. Microw. Theory Techn.*, vol. 69, no. 6, pp. 2854–2869, Jun. 2021.

[47] N. S. Mannem et al., "A 25–34-GHz eight-element MIMO transmitter for keyless high throughput directionally secure communication," *IEEE J. Solid-State Circuits*, vol. 57, no. 5, pp. 1244–1256, May 2022.

[48] H.-C. Park et al., "Single transformer-based compact Doherty power amplifiers for 5G RF phased-array ICs," *IEEE J. Solid-State Circuits*, vol. 57, no. 5, pp. 1267–1279, May 2022.

Yaolong Hu (Graduate Student Member, IEEE) received the B.Eng. degree from Zhejiang University, Hangzhou, China, in 2018. He is currently pursuing the Ph.D. degree in electrical and computer engineering with Rice University, Houston, TX, USA.

From May 2022 to August 2022, he was an Analog Design Intern with Kilby Labs, Texas Instruments Inc., Dallas, TX, USA. His research interests include millimeter-wave integrated circuits and systems.

Mr. Hu was a recipient of the ISSCC Travel Grant Award in 2024, the IEEE Custom Integrated Circuits Conference (CICC) Best Student Paper Award in 2021, and the IEEE International Microwave Symposium (IMS) Advanced Practice Paper Award Finalist in 2021. He was also a corecipient of the IEEE RFIC Symposium Best Industry Paper Award Finalist in 2023. He has served as a reviewer for the IEEE TRANSACTIONS ON MICROWAVE THEORY AND TECHNIQUES (TMTT) and the IEEE TRANSACTIONS ON CIRCUITS AND SYSTEMS II: EXPRESS BRIEFS (TCAS-II).

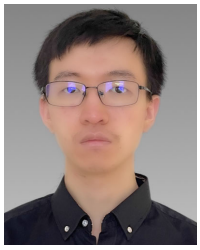

Xiaohan Zhang (Graduate Student Member, IEEE) received the B.S. degree from Tsinghua University, Beijing, China, in 2019. He is currently pursuing the Ph.D. degree in electrical and computer engineering with Rice University, Houston, TX, USA.

From August 2021 to May 2022, he was an Internship Student at Samsung Research America (SRA), Plano, TX, USA, working on sub-terahertz IC design. His research interests include millimeter-wave/sub-terahertz integrated circuits and systems for wireless communications, especially on power amplifiers and array architectures.

Mr. Zhang was a recipient of the 2023–2024 IEEE Solid-State Circuits Society (SSCS) Predoctoral Achievement Award, the ISSCC Travel Grant Award in 2023, the IEEE Radio Frequency Integrated Circuits (RFIC) Symposium Best Student Paper Award Finalist in 2022, and the IEEE Custom Integrated Circuits Conference (CICC) Best Student Paper Award in 2021. He was also a corecipient of the IEEE RFIC Symposium Best Industry Paper Award Finalist in 2023. He has served as a technical reviewer for the IEEE JOURNAL OF SOLID-STATE CIRCUITS (JSSC), IEEE TRANSACTIONS ON MICROWAVE THEORY AND TECHNIQUES (TMTT), IEEE MICROWAVE AND WIRELESS TECHNOLOGY LETTERS (MWTL), IEEE TRANSACTIONS ON CIRCUITS AND SYSTEMS I: REGULAR PAPERS (TCAS-I), and IEEE TRANSACTIONS ON CIRCUITS AND SYSTEMS II: EXPRESS BRIEFS (TCAS-II).

Taiyun Chi (Member, IEEE) received the B.S. degree (Hons.) from the University of Science and Technology of China (USTC), Hefei, China, in 2012, and the Ph.D. degree from Georgia Institute of Technology, Atlanta, GA, USA, in 2017.

He is currently an Assistant Professor with the Department of Electrical and Computer Engineering, Rice University, Houston, TX, USA, where he directs the Rice Integrated Systems and Electromagnetics (RISE) Laboratory. His research focuses on developing analog, RF, and millimeter-wave integrated circuits and systems for wireless communication, sensing, and neuro-engineering applications.

Dr. Chi is a Technical Program Committee (TPC) Member of the IEEE Custom Integrated Circuits Conference (CICC) and the International Microwave Symposium (IMS). His research group received the 2022 IEEE Radio Frequency Integrated Circuits (RFIC) Symposium Best Student Paper Award Finalist, the 2021 IEEE CICC Best Student Paper Award, the 2021 IEEE IMS Advanced Practice Paper Award Finalist, and the 2021 Texas Wireless Symposium Student Research Competition Award (First Place). He was also a recipient of the National Science Foundation (NSF) CAREER Award in 2023, the Rice School of Engineering Teaching and Research Excellence Award in 2023, the Sigma Xi Best Ph.D. Thesis Award (Georgia Tech Chapter) in 2018, the IEEE CICC Best Paper Award in 2017, the IEEE Solid-State Circuits Society (SSCS) Predoctoral Achievement Award in 2017, the Microwave Theory and Techniques Society (MTT-S) Graduate Fellowship for Medical Applications in 2016, and the USTC Guo Moruo Presidential Scholarship in 2012. He is the TPC Co-Chair for the IEEE Texas Symposium on Wireless and Microwave Circuits and Systems.